

What Vertical Mode Does the Altimeter Reflect? On the Decomposition in Baroclinic Modes and on a Surface-Trapped Mode

GUILLAUME LAPEYRE

Laboratoire de Météorologie Dynamique/IPSL, Ecole Normale Supérieure/CNRS, Paris, France

(Manuscript received 21 December 2007, in final form 1 April 2009)

ABSTRACT

This study is motivated by the ongoing debate on the dynamical properties of surface motions at mesoscales that are measured by altimetry [for sea surface height (SSH)] and microwave [for sea surface temperature (SST)]. The mesoscale signal obtained by the altimeter is often considered to be associated with the first baroclinic mode, but recent results indicate that SST spectra and surface kinetic energy spectra derived from SSH have the same slope, which is not consistent with this hypothesis. Moreover, baroclinic modes are associated by definition with vanishing buoyancy anomalies at the ocean surface, which is obviously not the case. Here a careful derivation of the vertical modes is done using the concepts of quasigeostrophic potential vorticity (QGPV) theory. Since the surface buoyancy can be interpreted as a Dirac function in PV, the traditional baroclinic modes have to be completed by a surface-trapped mode with no interior QGPV. The possible contribution of each mode is quantified in a realistic simulation of the North Atlantic Ocean. The surface mode is found to give the largest contribution in terms of surface energy in most of the Atlantic. Its relative importance compared to the other modes is determined at first order by the large-scale forcing of PV and surface buoyancy. These results emphasize the necessity for a new interpretation of satellite measurements of sea surface temperature or height.

1. Introduction

Satellite measurements of surface signals such as sea surface height (SSH) and sea surface temperature (SST) are now routinely available with a relatively good global coverage in space and time and provide information on the surface oceanic circulation. However, the interior circulation is far less documented at a weekly time scale because only few measurements are available. Relating the surface signal to the interior signal is therefore needed to better assimilate the satellite signals in operational models and to propagate the surface information into the interior. This propagation could be done by creating additional observations using the relationship between the surface signal and the interior. Some attempts have been made in that direction using vertical EOFs (e.g., De Mey and Robinson 1987), or inverting a uniform potential vorticity (PV) distribution and using the surface streamfunction to constraint the flow at depth (Haines 1991);

however, we still need dynamical constraints to improve the method. This step may be not necessary if the assimilation process is fully able to create a dynamically coherent field in the vertical.

It is generally thought that mesoscale motions at the ocean surface are strongly related to the first baroclinic mode. This conjecture was proposed by Stammer (1997), who observed that the length scale of zero crossing of the spatial autocorrelation of the SSH was proportional to the first Rossby deformation radius. According to Stammer (1997), this “suggests that first-mode processes dominate observed SSH fluctuations.” In addition, Wunsch (1997) examined the partition of kinetic energy obtained by current meters into vertical modes and showed that “surface kinetic energies are dominated by the first baroclinic mode.” These results from direct observations were confirmed, in some manner, by numerical simulations. Smith and Vallis (2001) showed, in simulations of multilayer quasigeostrophic turbulence, that the first baroclinic mode gives a contribution greater than the barotropic mode contribution to the surface mesoscale kinetic energy for a stratification with a thermocline. This was not the case for a stratification with constant Brunt–Väisälä frequency. In

Corresponding author address: G. Lapeyre, LMD/IPSL, Ecole Normale Supérieure, 24 Rue Lhomond, 75005 Paris, France.
E-mail: glapeyre@lmd.ens.fr

addition, Scott and Arbic (2007) showed that the surface energy budget was very similar to the first baroclinic mode energy budget of a two-layer model of quasigeostrophic turbulence with equal and unequal layers. This result was consistent with analysis of the spectral kinetic eddy fluxes from altimetry (Scott and Wang 2005) and from a numerical simulation in an ocean general circulation model (OGCM) (Schlösser and Eden 2007).

However, numerical simulations of quasigeostrophic turbulence by Smith and Vallis (2001) and Scott and Arbic (2007) have not considered the presence of surface density anomalies. As a result, the potential energy in the upper layers (that can be represented by SST variance) has a steeper spectrum than kinetic energy. This is contrary to recent results obtained with high-resolution simulations of primitive equations (Klein et al. 2008), OGCM simulations (Isern-Fontanet et al. 2008), and analysis of satellite data (Isern-Fontanet et al. 2006) that showed that SST and KE spectra have the same slope at mesoscales. To explain such property, the surface quasigeostrophy (SQG) theory was invoked by these authors. In SQG, there are no interior potential vorticity anomalies, and the surface flow field is driven by the time evolution of surface density anomalies. This means that upper oceanic layers are in a different dynamical balance from the interior layers, as was first observed by Lapeyre and Klein (2006).

To clarify the discrepancies between the different studies, it is necessary to determine if the surface signal is related to an interior baroclinic mode or to a mode related to SQG. Using theoretical results of Lapeyre and Klein (2006), a decomposition of the mesoscale dynamics of a numerical simulation of the North Atlantic Ocean into vertical baroclinic modes and the SQG mode is performed. The model used here is the Parallel Ocean Program (POP) model at $1/10^\circ$ (Smith et al. 2000; Bryan et al. 2007), which resolves the mesoscale dynamics with realistic forcing and is suitable for this type of study. A quantitative comparison with Ocean Topography Experiment (TOPEX) altimeter data has indeed shown that it had similar characteristics in terms of energy and length scales (Brachet et al. 2004). In section 2, the vertical modes are carefully derived with the introduction of a surface-trapped mode that satisfies the surface boundary condition and corresponds to SQG dynamics. The decomposition is then performed and examined in detail for three regions with high mesoscale activity in the North Atlantic Ocean in section 3. The contributions of the surface and interior modes for the surface signal are then determined. Results are discussed at a basin scale in section 4, and conclusions drawn in section 5.

2. Posing the problem of the vertical decomposition

In physical oceanography, the standard method to obtain the baroclinic modes is to linearize the quasigeostrophic equations of motion (Pedlosky 1987). We first introduce the QG potential vorticity (QGPV):

$$\text{PV} = f + \nabla^2 \psi + \frac{\partial}{\partial z} \left(\frac{f_0^2}{N^2} \frac{\partial \psi}{\partial z} \right) \quad (1)$$

and surface buoyancy:

$$b_s = f_0 \frac{\partial \psi}{\partial z} \Big|_{z=0}, \quad (2)$$

where $b = -g\rho/\rho_0$ is buoyancy anomaly and ρ a density anomaly, ψ is the streamfunction, f the Coriolis parameter (f_0 its value at a given latitude), and N the Brunt-Väisälä (or buoyancy) frequency. The QG equations are

$$\frac{\partial \text{PV}}{\partial t} + \mathbf{u} \cdot \nabla \text{PV} = 0 \quad (3)$$

for the interior PV and

$$\left(\frac{\partial}{\partial t} + \mathbf{u}_s \cdot \nabla \right) b_s = 0 \quad (4)$$

for the surface buoyancy b_s . In these equations, \mathbf{u} and \mathbf{u}_s are respectively horizontal velocity $\mathbf{u} = (-\partial\psi/\partial y, \partial\psi/\partial x)$ and ocean surface velocity.

If we linearize (3) and (4) around a time-independent zonal flow $U(z)$ in thermal wind balance, we find

$$\begin{aligned} \left(\frac{\partial}{\partial t} + U \frac{\partial}{\partial x} \right) \left[\nabla^2 \psi + \frac{\partial}{\partial z} \left(\frac{f_0^2}{N^2} \frac{\partial \psi}{\partial z} \right) \right] \\ + \frac{\partial \psi}{\partial x} \left[\beta - \frac{\partial}{\partial z} \left(\frac{f_0^2}{N^2} \frac{\partial U}{\partial z} \right) \right] = 0 \end{aligned} \quad (5)$$

and

$$\left(\frac{\partial}{\partial t} + U|_{z=0} \frac{\partial}{\partial x} \right) \frac{\partial \psi}{\partial z} \Big|_{z=0} - \frac{\partial \psi}{\partial x} \Big|_{z=0} \frac{\partial U}{\partial z} \Big|_{z=0} = 0. \quad (6)$$

Here ψ is a streamfunction anomaly. Developing in normal modes, we have $\psi = G(z) \exp(ikx + ily - i\omega t)$, which gives an eigenvalue problem:

$$\begin{aligned} (\omega - Uk) \left[-(k^2 + l^2)G + \frac{\partial}{\partial z} \left(\frac{f_0^2}{N^2} \frac{\partial G}{\partial z} \right) \right] \\ - kG \left[\beta - \frac{\partial}{\partial z} \left(\frac{f_0^2}{N^2} \frac{\partial U}{\partial z} \right) \right] = 0 \end{aligned} \quad (7)$$

and

$$(\omega - kU|_{z=0}) \frac{\partial G}{\partial z} \Big|_{z=0} + kG|_{z=0} \frac{\partial U}{\partial z} \Big|_{z=0} = 0, \quad (8)$$

where ω is the eigenvalue. Then we obtain eigenfunctions G , which depend on wavenumbers k and l and the (complex) frequency ω (Pedlosky 1987). Depending on the imaginary part of ω , one can have stable or unstable solutions of the instability problem. The vertical modes G can be divided into three classes: “surface trapped”; “internal-maximum trapped” (i.e., modes intensified at middepth); and “deep sea confined” (i.e., modes intensified near the ocean bottom) following Beckmann (1988).

This linear instability problem can be further simplified using the assumptions of a flat bottom and no mean shear (Flierl 1978; Gill 1982; Chelton et al. 1998). In that case, the vertical modes [noted $F_j(z)$ in the following] do not depend anymore on k, l , and ω . They satisfy a Sturm–Liouville equation with eigenvalues $-\lambda_j^{-2} \geq 0$,

$$\frac{\partial}{\partial z} \left(\frac{f_0^2}{N^2} \frac{\partial F_j}{\partial z} \right) = -\lambda_j^{-2} F_j, \quad (9a)$$

and

$$\frac{\partial F_j}{\partial z} \Big|_{z=0} = 0, \quad (9b)$$

where λ_j are the Rossby deformation radii. These modes can be used as an orthonormal basis of the space of solutions so that

$$\psi(x, y, z) = \sum_{j=0}^{\infty} \varphi_j(x, y) F_j(z). \quad (10)$$

An inherent property of such a decomposition is that the absence of a mean shear precludes surface buoyancy anomalies because

$$\frac{\partial}{\partial t} \frac{\partial \psi}{\partial z} = 0 \quad (11)$$

at $z = 0$ from (6). Therefore, baroclinic modes are not a complete basis in all situations. McWilliams (1976) proposed a method to modify the normal modes to include a surface shear, but his method seems difficult to generalize.

An important question is how to extend the linear modes to the nonlinear and nonstationary case so as to analyze OGCM simulations or real observations. As

shown by Chelton et al. (2007) using altimetry and Siegel et al. (2001) using idealized numerical simulations, the ocean at mesoscales is full of strongly nonlinear vortices. First, it is difficult to define a time-independent flow from observations. Even in this case, this flow would be spatially nonuniform so that the computation of the modes would be impractical. Because the mesoscale kinetic energy is much larger than kinetic energy of the large-scale currents, it can also be argued that the linear approximation is not valid anymore. Another difficulty is that each class of vertical modes is defined for a particular surface condition. As a result, the decomposition in vertical modes will not be complete because a part of the solution cannot be represented. For an infinite sum of modes, it can be shown that the error is localized in a delta function sheet at the ocean surface. However, the time evolution of this delta function sheet is precluded because of the surface condition, which makes the problem ill-posed. Dealing with real data or with numerical models, only a finite set of modes can be computed and the error can be important. For these reasons, the issue of vertical modes needs to be addressed differently.

Following Charney (1971), Hoskins et al. (1985), and Bishop and Thorpe (1994), a more direct and dynamically consistent method can be used to derive these modes. It is based on the principle of potential vorticity inversion. If we do not consider the time-evolution equations (3) and (4) but only the PV and surface density equations (1) and (2), we may try to estimate the velocity field from the PV field. The linear operator in (1) that passes from streamfunction to the PV anomaly $PV' = PV - f$ is elliptic in general (because $N^2 > 0$ in stable stratification). It is then possible to invert (1) under proper boundary conditions (in particular at the ocean surface) to obtain the streamfunction field. As shown by Bretherton (1966), the surface buoyancy plays the same role as an interior PV if it is replaced with a Dirac delta function distribution in the PV equation. The mathematical problem is thus to invert (1) and (2), which can be solved by splitting the solution ψ into two parts, ψ_{int} and ψ_{sur} [see Lapeyre and Klein (2006) for more details]:

$$\begin{aligned} \nabla^2 \psi_{\text{int}} + \frac{\partial}{\partial z} \left(\frac{f_0^2}{N^2} \frac{\partial \psi_{\text{int}}}{\partial z} \right) &= PV' \\ \frac{\partial \psi_{\text{int}}}{\partial z} \Big|_{z=0} &= 0 \\ \frac{\partial \psi_{\text{int}}}{\partial z} \Big|_{z=-H} &= 0 \end{aligned} \quad (12)$$

and

$$\nabla^2 \psi_{\text{sur}} + \frac{\partial}{\partial z} \left(\frac{f_0^2}{N^2} \frac{\partial \psi_{\text{sur}}}{\partial z} \right) = 0 \quad (13)$$

$$\frac{\partial \psi_{\text{sur}}}{\partial z} \Big|_{z=0} = \frac{b_s}{f_0}$$

$$\frac{\partial \psi_{\text{sur}}}{\partial z} \Big|_{z=-H} = 0.$$

We choose to neglect the density anomalies at the bottom of the ocean ($z = -H$) since they are small in general. These two equations are related to two different problems: ψ_{int} is associated with interior PV anomalies with no surface buoyancy anomalies. It corresponds to the standard paradigm of interior PV layers in the Phillips model of baroclinic instability. For this balance, the available potential energy (APE) spectrum is steeper than the kinetic energy (KE) spectrum in the upper oceanic layers. On the other hand, ψ_{sur} is associated with the surface buoyancy anomaly with uniform interior PV. It corresponds to the standard paradigm of surface anomalies in the Eady problem of baroclinic instability and to surface QG dynamics (Held et al. 1995). This dynamical balance is characterized by the same spectral slopes for KE and APE in the upper oceanic layers. The typical time scale of SQG flows is proportional to the inverse of the surface vorticity, in the range from 1 to 5 days. This is more rapid than the interior dynamics; however, in the case of interaction between the surface and the interior, one could think that the coupling will slow down the surface dynamics.

The first PV inversion problem satisfies simple boundary conditions (vanishing surface buoyancy). We recognize a Sturm–Liouville operator in the vertical and can use the theory of elliptic operators. The solution uses the standard baroclinic modes F_j ,

$$\nabla^2 \phi_j - \lambda_j^{-2} \phi_j = \int_{-H}^0 \text{PV}'(x, y, z) F_j(z) dz, \quad (14)$$

with

$$\psi_{\text{int}}(x, y, z) = \sum_{j=0}^{\infty} \phi_j(x, y) F_j(z). \quad (15)$$

The vertical integral clearly demonstrates that ψ_{int} is driven (or forced¹) by the interior dynamics. Then the modes F_j can be called “interior modes.” The solution of the homogeneous problem (13) is

$$\hat{\psi}_{\text{sur}}(\mathbf{k}, z) = E(K, z) \frac{\hat{b}_s(\mathbf{k})}{f_0}, \quad (16)$$

where the caret denotes horizontal Fourier transform, \mathbf{k} is the horizontal wavevector, and K is its modulus. For each wavenumber \mathbf{k} , $E(K, z)$ satisfies

$$-K^2 E + \frac{\partial}{\partial z} \left(\frac{f_0^2}{N^2} \frac{\partial E}{\partial z} \right) = 0, \quad (17)$$

with $\partial E / \partial z = 1$ at $z = 0$ and $\partial E / \partial z = 0$ at $z = -H$. There is no solution for $K = 0$. From (16), we see that ψ_{sur} only depends on the surface buoyancy and stratification N^2 . It does not depend on the interior flow. This is why we call the associated mode E a “surface mode.” The solution is surface intensified and decreases with depth. As an example, in the case of constant N^2 for an ocean with infinite depth, the solution is

$$E(K, z) = \frac{f_0}{NK} \exp\left(\frac{NKz}{f_0}\right). \quad (18)$$

This is a SQG solution that decays exponentially with depth. Smaller horizontal structures (larger K) have smaller vertical decay scales, which preserve the 3D isotropy. A property of such a system is that buoyancy and kinetic energy have the same spectra at the ocean surface. More details on SQG dynamics can be found in Held et al. (1995) and Lapeyre and Klein (2006).

Instead of using the decomposition in baroclinic modes to solve (7) and (8), the eigenvalues h_n of (7) can be found replacing $\partial_z(f_0^2 N^{-2} \partial_z G)$ by $-f_0^2 G / gh_n$ and using a proper horizontal boundary condition. Then, the vertical structure of G can be solved for each h_n . This method is described by Philander (1978) and Frankignoul and Muller (1979). One obtains an oscillatory solution in the vertical for positive h_n and surface-intensified solution for negative h_n [these are called “negative depth eigenfunctions” following Philander (1978)]. However, these solutions are different from the surface mode defined by (17) because the depth eigenvalues h_n depend entirely on frequency ω . On the contrary, the vertical scale of the surface mode $E(K, z)$ depends only on f_0 , N , and the horizontal wavenumber. It is defined virtually for all scales and then projected on buoyancy following (16). Even if the PV (or the surface buoyancy) is externally forced in time, one can in principle decompose any solution on the SQG and the baroclinic modes. This is, indeed, demonstrated by Frankignoul and Muller (1979).

Numerical simulations of oceanic QG turbulence have not considered motions associated with ψ_{sur} because they all assume no buoyancy anomaly at the surface

¹ The term *forcing* is used because it enters the rhs of the elliptic equation (14).

(McWilliams and Chow 1981; Hua and Haidvogel 1986; Smith and Vallis 2001). The same shortcoming is also encountered when analyzing in situ observations (McWilliams et al. 1986; Wunsch 1997; among others). Only recent studies of stratified turbulence (Lapeyre and Klein 2006; Lapeyre et al. 2006; Klein et al. 2008) have highlighted the important role of surface buoyancy anomalies for the dynamics of upper oceanic layers. The similar role of the tropopause was also shown to be important for the tropospheric dynamics (Tulloch and Smith 2006, 2009b).

Because the baroclinic vertical modes F_j are not able to represent motions associated with ψ_{sur} , it can be argued that these modes are “incomplete” in describing the dynamics. Both buoyancy and streamfunction need to be dynamically decomposed at the same time to maintain the thermal wind balance. As a result, part of the total energy may not be captured. The argument is similar to the ones of Dutton (1974), Held et al. (1985), and Tung and Welch (2001): in a modal decomposition associated with a Sturm–Liouville problem, the boundary conditions are crucial for the existence and completeness of the eigenvectors of the problem. Any function that satisfies the same boundary condition as the eigenvectors of the Sturm–Liouville problem will expand on the basis formed by these eigenvectors. If a function does not satisfy the same boundary condition, a continuous spectrum of eigenvalues is necessary to close the problem. If the modes satisfy homogeneous boundary conditions and if the solution that we seek satisfies inhomogeneous boundary conditions, the convergence of the expansion in modes is not uniform (Held et al. 1985).

To complete the interior modes F_j , we thus need to add a surface-trapped solution [depending on $E(K, z)$]. Both types of modes (interior and surface) have a signature at the surface in terms of a velocity field, but only the surface-trapped solution has a signature in density at the surface. The question then arises whether the signal seen by the altimeter (or other satellite instruments that examine the surface dynamics) is related to the interior dynamics. The preceding discussion suggests that it might either be attributed to baroclinic modes F_j or the surface-intensified mode E .

3. Application to an OGCM simulation

To answer the preceding question, the output of a realistic simulation of the North Atlantic Ocean is examined. The numerical model used here is the POP model with a resolution of $1/10^\circ$ (in Mercator grid) over a stretched vertical grid of 40 levels, and the simulation is forced with realistic winds and heat fluxes [see Isern-

Fontanet et al. (2008) for more details]. The different variables are daily averaged for a particular day in January 2002. Other days were tested, and results were found to be very similar. The daily average filters a large part of near-inertial waves so that only the balance part of the flow is retained.

a. Numerical method

The decomposition in vertical modes was performed on domains of $10^\circ \times 10^\circ$ over the North Atlantic Ocean between 30° and 50°N , 70° and 10°W . In each domain, data are projected using a Mercator projection and interpolated onto a grid of 256×256 points. Then each domain is made periodic by doubling its size to a grid of 512×512 using mirror symmetry for buoyancy in x and y . The velocity is split in a domain-averaged value and an anomaly (dependent on x and y). In the same way as density, the velocity anomaly is made periodic using mirror symmetry, but we reverse its sign adequately to preserve the thermal wind balance. The final velocity (sum of the domain-averaged value and the new anomaly) is then periodic and continuous; only its horizontal derivatives are discontinuous. An exponential filter is used to smooth spectrally the vorticity field (Canuto et al. 1988).

To create missing data on islands and seamounts, the following procedure was applied: at each level, points where the bathymetry outcrops the level are replaced by a weighted mean over a region of 2° latitude by 2° longitude. The weight decays exponentially with the square of the distance. The velocity field obtained by this method is continuous on the horizontal, which allows one to use horizontal Fourier transforms (other details are provided in the appendix). The results are not very sensitive to the details of the method as long as the bottom buoyancy anomalies are weak.

A “complete” decomposition of a geostrophic flow ψ consists of finding coefficients $\hat{\gamma}(\mathbf{k})$ and $\hat{\alpha}_j(\mathbf{k})$ that satisfy

$$\hat{\psi}(\mathbf{k}, z) = E(K, z)\hat{\gamma}(\mathbf{k}) + \sum_{j=0}^n F_j(z)\hat{\alpha}_j(\mathbf{k}). \quad (19)$$

The first term on the rhs corresponds to the surface mode, whereas the sum corresponds to the interior modes (barotropic and baroclinic). The decomposition (19) will be considered complete since it takes into account the surface condition. (Details concerning the technical aspect of the decomposition are given in the appendix.) The complete decomposition has been validated on two test cases: one with a surface mode and a baroclinic mode with a constant N^2 and the other with an exponential stratification profile with only one baroclinic mode (not shown).

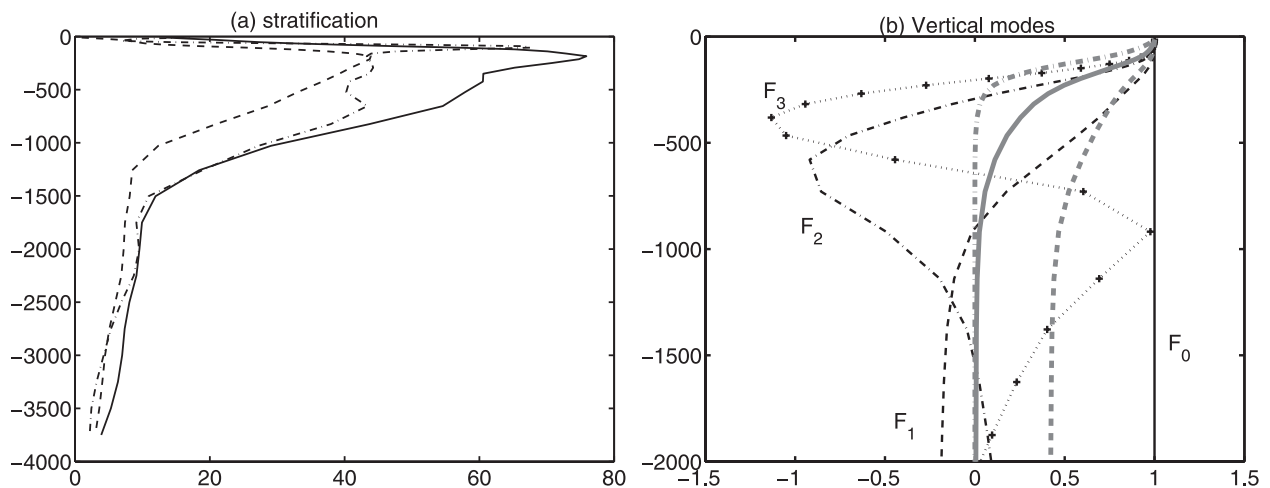


FIG. 1. (a) Vertical profile of N/f_0 for three oceanic regions: 1) GS (continuous line), 2) NAD (dashed), and 3) AC (dashed-dotted). (b) First four interior modes $F_j(z)$ (black line) and surface mode $E(K = 2\pi l, z)$ for $l = 100$ km (thick gray line), $l = 550$ km (thick dashed gray line), $l = 30$ km (thick dashed-dotted gray line). The different curves have been normalized so that $\psi = 1$ at $z = 0$. The modes were computed for the GS region.

An incomplete decomposition consists of finding coefficients $\hat{\beta}_j(\mathbf{k})$ that satisfy

$$\hat{\psi}(\mathbf{k}, z) = \sum_{j=0}^n F_j(z) \hat{\beta}_j(\mathbf{k}). \quad (20)$$

The solution of such a problem will not satisfy the surface condition since $\partial F_j/\partial z = 0$ at the surface. The coefficients $\hat{\beta}_j(\mathbf{k})$ can be found by the relation

$$\hat{\beta}_j(\mathbf{k}) = \int_{-H}^0 F_j(z) \hat{\psi}(\mathbf{k}, z) dz. \quad (21)$$

The two decompositions are performed using $n = 7$, which gives sufficiently good reconstruction as shown later.

Throughout the North Atlantic Ocean, similar properties for the decomposition in vertical modes are observed. For this reason, three subregions where the mesoscale activity is important are studied in detail: the Gulf Stream (GS), the North Atlantic Drift (NAD), and the Azores Current (AC). Properties at a more global scale will be examined in section 4. Before describing the main results, the buoyancy frequency is shown in Fig. 1a for these three regions. In the Gulf Stream and the Azores Current, a seasonal thermocline is present around 200–300 m. The main thermocline is located at deeper levels ranging from 400 m for the NAD to 800 m for the AC. Surface layers of each region are weakly stratified because of the winter conditions.

Figure 1b represents the first four vertical modes F_j (for $j = 0, 1, 2, 3$) and the surface mode $E(K, z)$ (for three different wavelengths $2\pi K^{-1}$) computed for the Gulf

Stream stratification. The surface mode was computed with a varying N^2 and with a bottom boundary condition, $\partial E/\partial z = 0$. The vertical profiles are quite typical and do not change qualitatively for other oceanic regions (not shown). The first baroclinic mode corresponds to a Rossby deformation radius of 31 km and has its zero crossing at 900 m. The second baroclinic mode has a deformation radius of 13 km with two zero crossings: one at 300 m and another at 1540 m. The first seven baroclinic modes are intensified in the first 2000 m (not shown) owing to the presence of the thermocline. The surface mode $E(K, z)$ is also intensified in the first 1000 m for wavelengths between 30 and 550 km and decays with depth. Smaller wavelengths are associated with greater vertical decay rates, as consistent for a SQG solution with constant N^2 [see Eq. (18)]. Also, the presence of a strong barotropic component for large wavelengths can be noted.

b. Region near the Gulf Stream

The first studied region is near the Gulf Stream, between 30° and 40°N , 70° and 60°W (boxes 9, 10, 13, and 14 in Fig. 10a), and has a high mesoscale activity with many eddy interactions between each other and with the large-scale current (see Fig. 4a). In particular, it has values of relative vorticity reaching $0.6f$. The kinetic energy is intensified at the surface and decays rapidly with depth in the first 500 m (Fig. 2a). The buoyancy rms at mesoscale (for which wavelengths longer than 400 km have been filtered) has a maximum just below the mixed layer (ML) at 200 m and decays more smoothly with depth than KE (Fig. 3a). These results confirm that the mesoscale activity is concentrated in the upper ocean, which may be

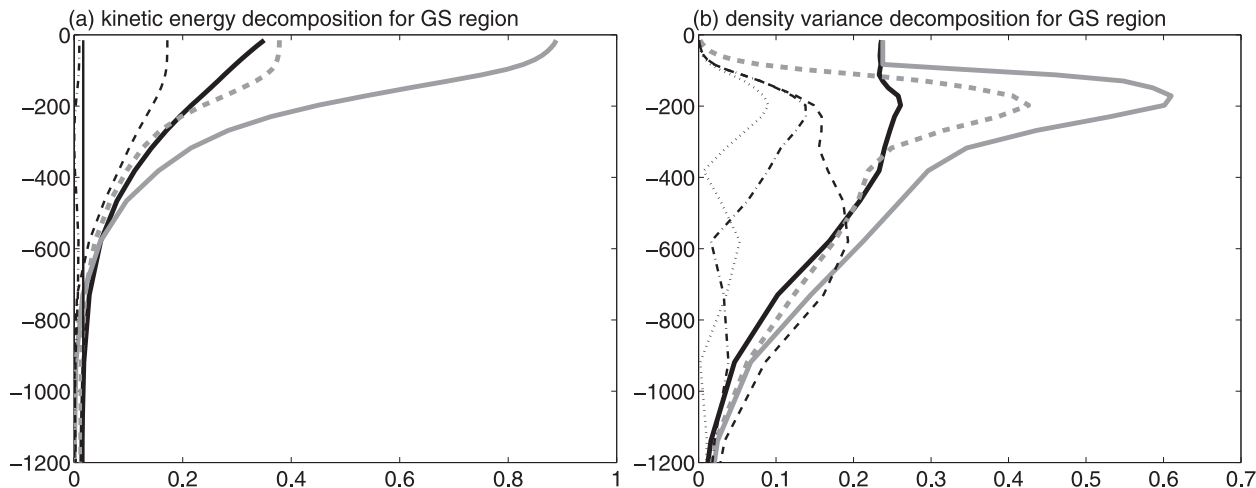


FIG. 2. (a) Vertical profile of the mean KE (thick black line), KE of surface mode (thick gray line), and KE of the sum of interior modes (thick dashed gray line): barotropic mode (black continuous line), first baroclinic mode (dashed black line), second baroclinic mode (black dashed-dotted line). (b) As in (a), but for density variance. Dotted line represents the third baroclinic mode.

attributed to the presence of a strong thermocline (Hua and Haidvogel 1986; Smith and Vallis 2001).

The ability of the complete and incomplete decompositions to fully describe the dynamics can be analyzed by comparing the total flow and its reconstruction using both decompositions. Both methods are able to correctly represent the mean kinetic energy except in the first 80 m (not shown). The reconstruction of the buoyancy (as revealed by its rms) using the complete method seems relatively good below the mixed layer and at the surface (Fig. 3a). However, it does not give the right variance at the bottom of the mixed layer. The situation is worse for the incomplete method: the buoyancy anomaly reconstruction vanishes at the surface and is quite small in the first 100 m so that there is a systematic error owing to the reconstruction down to 400 m. This

error can still be detected down to 1100 m (on the contrary of the complete method, which gives the right buoyancy rms below 500 m). This is also confirmed by the rms of the difference of the true buoyancy with its reconstruction (Fig. 3b) since the complete reconstruction gives much smaller rms for the first 300 m than the incomplete reconstruction. The inability of the incomplete method in reconstructing the buoyancy field demonstrates that the surface mode is crucial to fully describe the dynamics, particularly at the ocean surface.

The kinetic energy of the different vertical modes (interior and surface) can be separately evaluated at different depths to determine their relative importance. A caveat is that the sum of the surface kinetic energy of each mode is not the surface kinetic energy of the sum of the modes. Indeed, from (19), it can be seen that

$$\begin{aligned}
 KE(z) &= \frac{1}{2} \int K^2 |\hat{\psi}(\mathbf{k}, z)|^2 K dK = \frac{1}{2} \int K^2 E^2(K, z) |\hat{\gamma}(\mathbf{k})|^2 K dK + \frac{1}{2} \int \sum_{j=0}^n F_j^2(z) K^2 |\hat{\alpha}_j(\mathbf{k})|^2 K dK \\
 &+ \frac{1}{2} \int \sum_{j=0}^n F_j(z) K^2 E(K, z) \text{Re}[\hat{\gamma}(\mathbf{k}) \hat{\alpha}_j(\mathbf{k})^*] K dK + \int \sum_{i \neq j} F_i(z) F_j(z) \text{Re}[\hat{\alpha}_i(\mathbf{k}) \hat{\alpha}_j(\mathbf{k})^*] K dK, \quad (22)
 \end{aligned}$$

where (*) is the complex conjugate. The difference between the total KE and the sum of the KE of each vertical mode is equal to the two last terms of (22). These terms represent the correlation between different vertical modes and are nonzero in general. As can be seen in Fig. 2a, the kinetic energy of the surface mode in the Gulf Stream region dominates in the first 600 m and is twice as large as the observed kinetic energy. The first baroclinic mode represents the second largest contribution, which is

as large as the observed KE. In fact, as shown in Table 1, the first baroclinic and the surface modes are anticorrelated (considering their zonal or meridional velocity fields) so that their contributions cancel each other. This anticorrelation explains why their energy is larger than the observed KE at the ocean surface. The decomposition of the buoyancy variance (Fig. 2b) shows that the surface mode dominates the signal down to 600 m. The interior modes vanish at the surface but are quite important below

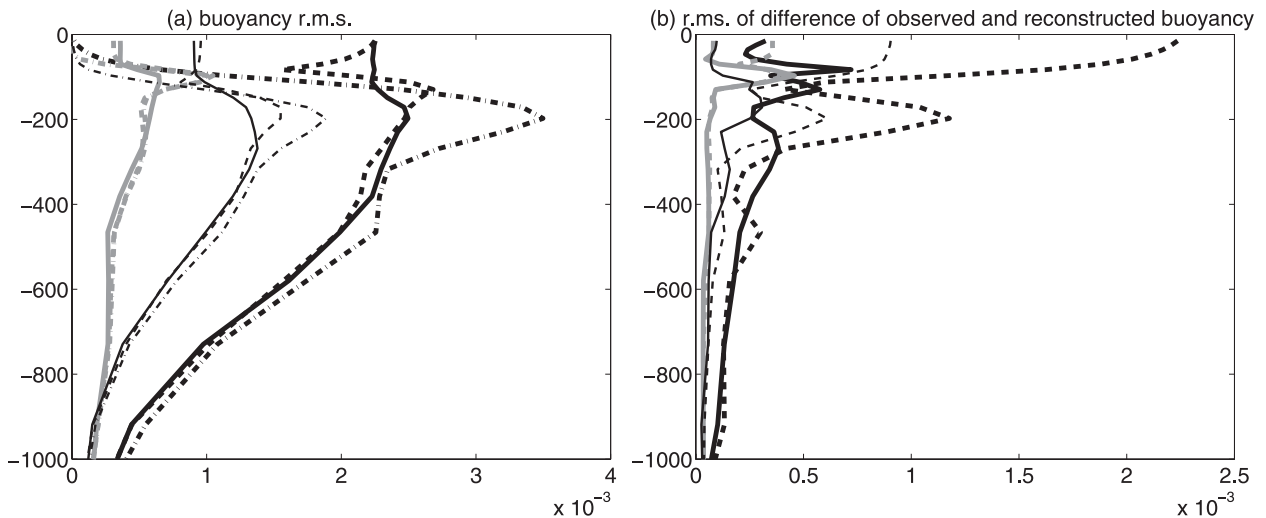


FIG. 3. (a) Vertical profile of the buoyancy rms (scales larger than 400 km have been filtered) for the reconstruction using complete (dashed) and incomplete (dashed-dotted) decomposition in the GS region (thick black curve), the AC region (thick gray curve), and the NAD region (thin black curve). (b) Vertical profile of the rms of the difference of reconstruction using complete (solid) and incomplete (dashed) decomposition method for the three oceanic regions.

150 m, that is, below the mixed layer. The buoyancy variance is partitioned relatively evenly between the different baroclinic modes between 100 and 300 m. Below 300 m, it is the first baroclinic mode that dominates.

To confirm the importance of the surface mode, the spatial fields at the surface can be examined. Figure 4 shows that the surface mode captures a large fraction of the mesoscale signal in relative vorticity, overestimating it particularly at small scales. It has a high correlation (0.80) with the true vorticity at the surface (Table 1). The first baroclinic mode is smaller and tends to diminish the high values of the surface mode (since it is of opposite sign in most regions and with a correlation of -0.42 with the true vorticity). The barotropic mode is negligible and captures larger-scale structures. Because the relative vorticity captures both mesoscale (100 km) and submesoscale (10 km) signals, it is also important to examine the characteristics of the velocity fields (arrows in Fig. 4). The velocities still show high correlations (0.79 and 0.81) between the model velocity (zonal or meridional) and its surface mode contribution (Table 1).

The surface KE spectra of the different vertical modes are shown in Fig. 5. The surface mode gives the largest contribution to the surface KE signal in the wavelength range from 30 km (corresponding to $K = 0.2 \text{ km}^{-1}$) to 800 km. At small scales, it decays faster than the true kinetic energy. The KE spectrum due to interior modes is also larger than the observed surface KE spectrum for all wavelengths. The partition between vertical modes shows that the first baroclinic mode is the most important one for scales smaller than 500 km. For scales larger

than 500 km, the barotropic mode is the most important one and cancels the surface mode contribution (but these scales are not properly resolved because we reach the size of the domain $800 \text{ km} \times 1200 \text{ km}$). The fact that the surface mode dominates in the mesoscale range (100–300 km) suggests that this mode will be detectable using SSH from altimetry.

c. North Atlantic Drift

The second studied region is in the North Atlantic Drift between 40° and 50°N , 40° and 30°W (boxes 31, 32, 35, and 36 in Fig. 10a) and is also active at mesoscales but with a weaker amplitude as the relative vorticity reaches only $0.3f$. We note the numerous eddies in this region (Fig. 6a). The kinetic energy of this region is still intensified at the

TABLE 1. Correlation coefficient of the different modes with the observed fields of vorticity, zonal and meridional velocities, at the ocean surface for the surface mode (SMOD), sum of interior modes (IMOD), the barotropic mode (BT), and first baroclinic mode (BC1).

Correlation	SMOD	IMOD	BT	BC1
Vorticity GS	0.80	-0.50	-0.36	-0.42
NAD	0.77	-0.32	-0.13	-0.18
AC	0.57	0.81	0.30	0.66
Zonal velocity GS	0.79	-0.38	-0.31	-0.33
NAD	0.81	-0.29	-0.39	-0.10
AC	0.58	0.88	0.53	0.82
Meridional velocity GS	0.81	-0.41	-0.29	-0.36
NAD	0.79	-0.15	-0.07	-0.16
AC	0.54	0.80	0.22	0.80

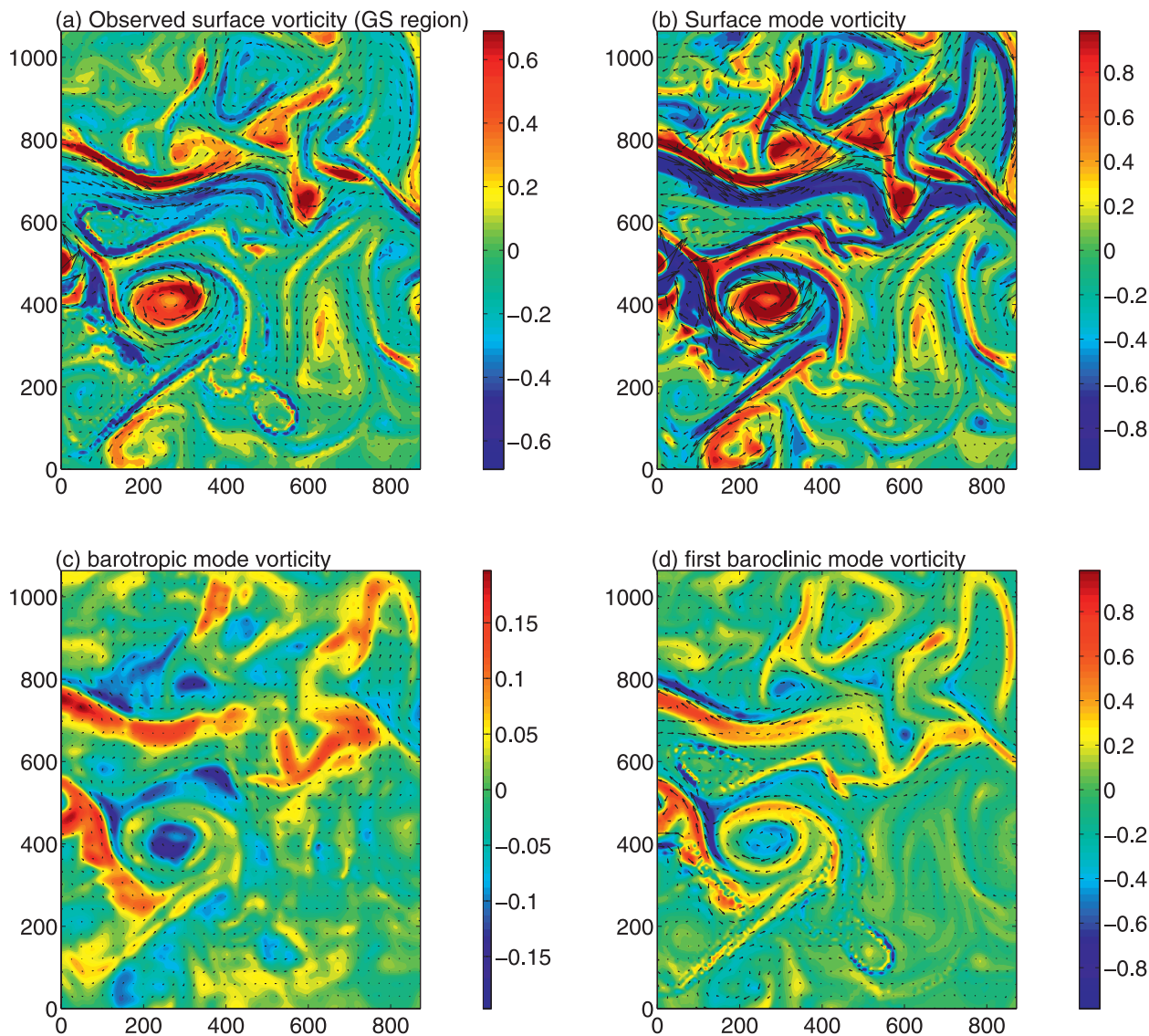


FIG. 4. Relative vorticity divided by f_0 (color) and horizontal velocities (vector arrows) (a) at the surface and for the (b) surface mode, (c) barotropic mode (complete decomposition), and (d) first baroclinic mode (complete decomposition). The figure corresponds to the GS region. The same velocity scale was used for the vector arrows in each figure.

surface (not shown), and the buoyancy rms is intensified at 200 m below the mixed layer (Fig. 3a). Concerning the reconstruction using the complete and incomplete decompositions, Fig. 3a shows that the rms of the buoyancy is better captured by the complete decomposition than by the incomplete decomposition, and differences can be observed down to 700 m. In the mixed layer (which is quite deep in this area, reaching 100-m depth), the complete decomposition gives correct rms values, which was not the case for the Gulf Stream area. The rms of the difference between the different reconstructions and the observed buoyancy (Fig. 3b) confirms that the complete method better represents the buoyancy field.

As shown in Fig. 6, the decomposition at the ocean surface is rather similar to the Gulf Stream region. The velocity and vorticity fields of the surface mode are more intensified than the observed fields and small scales are strongly enhanced. The first baroclinic mode is 180° out of phase with the surface mode, and the barotropic mode displays larger scale structures but of weaker intensity than the surface and first baroclinic modes. This qualitative picture is confirmed by the correlations computed at the ocean surface (Table 1), which are very similar to the correlations for the Gulf Stream region, except that the correlations of the first baroclinic mode with the surface flow are smaller. This is true for both the relative

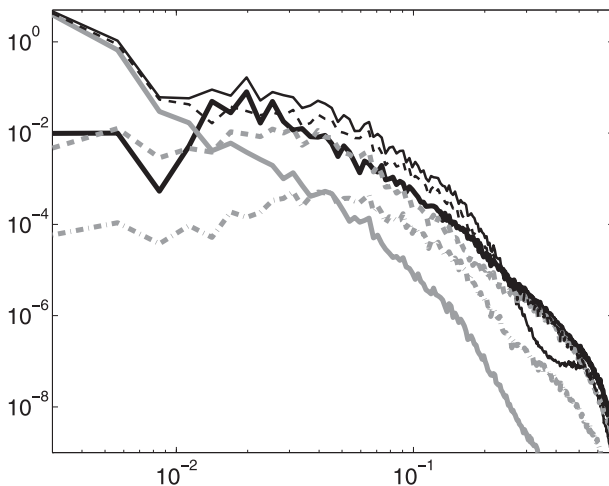


FIG. 5. Spectra of model KE (thick black line), surface mode KE (black solid line), interior modes KE (black dashed line) at $z = 0$ m in the GS region for the barotropic mode (thick gray line), the first baroclinic mode (gray dashed line), and the second baroclinic mode (gray dashed-dotted line).

vorticity and the velocity. The reason is that the KE of the surface mode and the observed KE have amplitude closer in the case of the NAD than in the case of the GS region (cf. KE spectra of Fig. 7 with those of Fig. 5). Henceforth, the interior modes do not need to strongly anticorrelate with the surface mode and thus with the observed fields. Apart from this difference, the surface KE spectra are very similar to the Gulf Stream region, with the surface mode prevailing between 30 and 500 km (Fig. 7).

d. Azores Current

The third region is an area between 30° and 40° N, 30° and 20° W in the Azores Current in the northeast Atlantic (boxes 33, 34, 37, and 38 in Fig. 10a). The relative vorticity shows modest activity at mesoscales with the presence of a few surface eddies and a large-scale eastward jet (Fig. 8a). Relative vorticity reaches values of $0.15f$. The kinetic energy is still intensified at the surface and decays with depth but with much smaller amplitude than in the two other regions. Figure 3a shows that the buoyancy rms has a much smaller amplitude as well. In this region, the complete and incomplete decompositions give almost the same buoyancy rms for all depths except in the shallow mixed layer (50 m). Indeed, the rms of the difference between the observed buoyancy and its complete or incomplete reconstruction shows a similar picture (Fig. 3b).

The decomposition in vertical modes (Fig. 8) gives a quite different result from the two other regions. The surface mode concentrates in small-scale frontal structures. However, it does not dominate the signal at the ocean surface and has the same amplitude as the first

baroclinic mode. The barotropic mode is still of weaker amplitude and at larger scales. Contrary to the other cases, the sum of interior modes better correlates with the observed vorticity and velocity fields at the ocean surface than the surface mode (Table 1). In addition, the first baroclinic mode is strongly correlated with the surface fields for each dynamical variable.

The surface KE spectra (Fig. 9) show that the interior modes dominate for almost all scales. Two exceptions are the larger scales where both surface and interior contributions have the same amplitude (but these scales are not correctly resolved because they are larger than the zonal size of the domain) and scales close to 30 km for which the surface mode becomes as important as the interior modes. This confirms the visual inspection of Fig. 8. The contribution of interior modes essentially comes from the first baroclinic mode, and it has the same amplitude as the surface mode for all wavelengths (except for scales larger than 600 km). As a result, both the surface mode and the first baroclinic mode positively contribute to the observed surface flow, as confirmed by the correlation coefficients in Table 1.

4. Interpretation at a basin scale

The three oceanic regions with high mesoscale activity display some features in common and some marked differences: For all three regions, the first baroclinic mode has greater KE than the other barotropic and baroclinic modes at the ocean surface. This result is similar to conclusions of Wunsch (1997) and Smith and Vallis (2001), who examined in situ data and simulations of QG turbulence, respectively. In addition, kinetic energy is intensified at the ocean surface and buoyancy anomalies are intensified below the mixed layer in each region. However, in two regions—the Gulf Stream and North Atlantic Drift—the surface mode has a more intense signal than the interior modes, whereas in the Azores Current, the first baroclinic mode is the larger mode. To see what happens at the basin scale, subdomains of size $6^{\circ} \times 5^{\circ}$ in Mercator grid in the North Atlantic were examined. We found that all subdomains have similar behavior as the three regions examined in section 3: Fig. 10 shows the ratio of the rms of relative vorticity of the interior modes to the rms of relative vorticity of the surface mode at the basin scale. The surface mode dominates in a large fraction of the Atlantic ocean (19 regions of size $6^{\circ} \times 5^{\circ}$ where the surface mode dominates versus 12 regions where the interior modes dominate). It is interesting to note that the surface mode dominates in the Gulf Stream and North Atlantic Current, whereas the interior modes dominate in the recirculating branch of the gyre (Azores Current and Portugal Current). One could argue

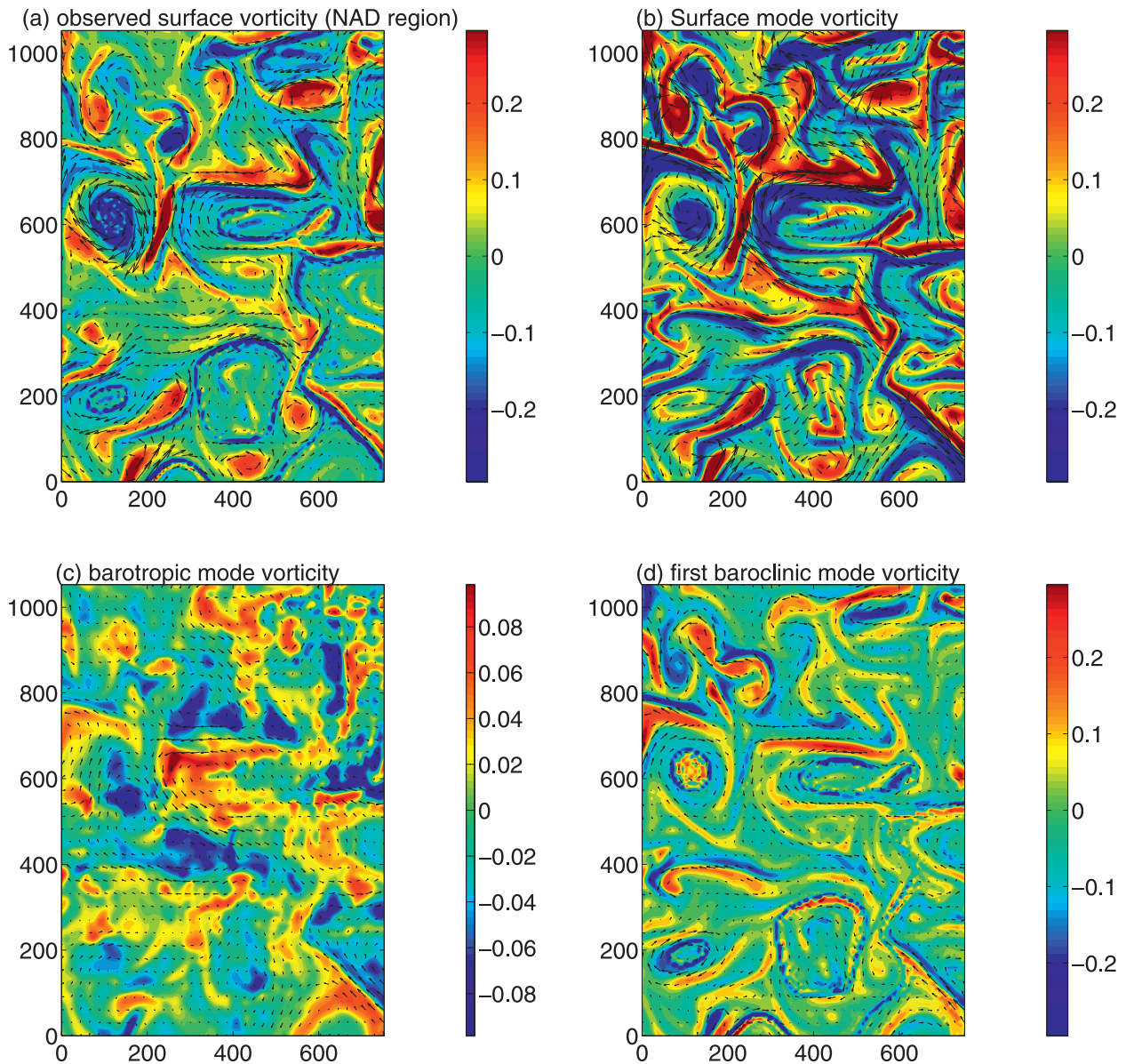


FIG. 6. As in Fig. 4, but for the NAD region.

that the vorticity will strengthen the surface mode signal because it is associated with submesoscale surface buoyancy anomalies. To have an accurate representation of what the altimeter might see, the meridional velocity was bandpassed filtered in the range 100–300 km. Figure 11a shows that in a large part of the North Atlantic, there is a correlation greater than 0.65 between the surface mode and the model meridional velocity. In the other regions, the first baroclinic mode correlates well with the meridional velocity (Fig. 11b). The consequence of this result is that the geostrophic velocities measured by the altimeter are most of the time due to the surface mode, not the first baroclinic mode.

To understand why the surface signal reflects the surface mode, we can use the analytical developments of Lapeyre and Klein (2006), who investigated the link between surface and interior dynamics. As explained in section 2, the PV inversion problem can be decomposed into two sub-problems: (12) and (13). Using the assumption that large-scale PV and surface buoyancy meridional gradients are the first source of mesoscale anomalies of PV and surface buoyancy, we can write the equations of anomalies as

$$\left(\frac{\partial}{\partial t} + \mathbf{u} \cdot \nabla\right) \text{PV}' = -v \frac{\partial \overline{\text{PV}}}{\partial y} \quad (23a)$$

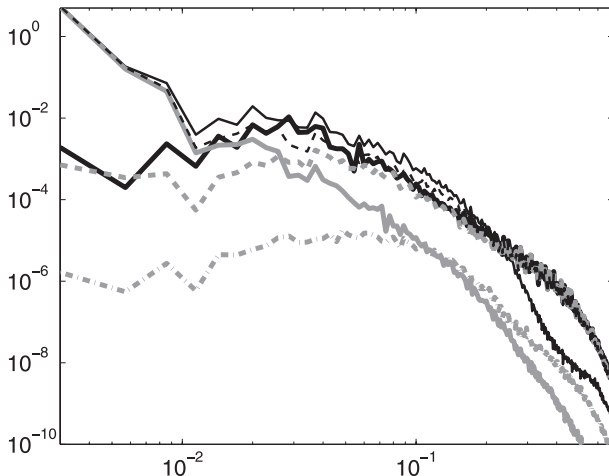


FIG. 7. Spectra of KE at the ocean surface for the NAD region; definitions as in Fig. 5.

and

$$\left(\frac{\partial}{\partial t} + \mathbf{u}_s \cdot \nabla\right) b'_s = -v_s \frac{\partial \bar{b}_s}{\partial y}, \quad (23b)$$

where PV' and b'_s are mesoscale anomalies and \overline{PV} and \bar{b}_s are large-scale variables. Considering that the velocity field has slow variations in the vertical (at least in the upper oceanic layers), Lapeyre and Klein (2006) derived a relation between the anomalies,

$$PV' \approx \frac{\partial_y \overline{PV}}{\partial_y \bar{b}_s} b'_s. \quad (24)$$

The reason is that the velocity field advects and stirs PV and surface buoyancy down their mean gradient in the same manner. If one assumes that the large-scale density gradient projects onto the first baroclinic mode [i.e., $\partial_y \bar{b} \approx F_1(z)B(y)$], then the large-scale PV gradient is proportional to the density gradient by the relation

$$\frac{\partial \overline{PV}}{\partial y} \approx \frac{\partial}{\partial z} \left(\frac{f_0}{N^2} \frac{\partial \bar{b}}{\partial y} \right) = \frac{\partial}{\partial z} \left[\frac{f_0 F_1(z)}{N^2} \right] \frac{\partial B(y)}{\partial y}. \quad (25)$$

So, a strong correlation exists between $\partial_y \overline{PV}$ and $\partial_y \bar{b}_s = F_1(z=0) \partial_y B$. The stirring process then drives the correlation that exists at large scale to small scales through the tracer cascades of interior PV and surface buoyancy and ultimately yields (24). Relation (24) has profound consequences when performing a PV inversion of Eqs. (12) and (13). As the forcing of the two equations is in phase, the inversion will create a phase relationship between ψ_{int} and ψ_{sur} .

To confirm this result, the regression of PV' on b'_s can be compared with the regression of $\partial_y \overline{PV}$ on $\partial_y \bar{b}_s$ (noted

as Γ for future use), choosing 400 km as the wavelength of separation between mesoscale and large scale (the fields have been respectively high-pass and low-pass filtered). Here, values below the ML base were chosen for surface QG buoyancy values because the buoyancy in the ML reflects either surface forcing or buoyancy below the ML, depending on the wind conditions (Klein and Hua 1990). This choice has the effect of increasing the correlation between PV' and b'_s , as expected. As shown in Fig. 12a, in the three oceanic regions, the two regressions qualitatively match each other for the first 1000 m. Relation (24) is further confirmed by the quite strong (positive or negative) correlations between interior PV anomalies and surface buoyancy anomalies (Fig. 12b). It can also be noted that the sign of the correlation is the same as the regression of $\partial_y \overline{PV}$ on $\partial_y \bar{b}_s$ (cf. Figs. 12a and 12b).

As a result, it can be expected that the sign and amplitude of Γ should impact the relation between ψ_{int} and ψ_{sur} . Figure 13a shows the scatterplot of Γ and the ratio of rms of vorticity due to ψ_{int} to the rms of vorticity due to ψ_{sur} evaluated at the ocean surface. For small values of $|\Gamma|$, the surface mode tends to have greater vorticity rms than the interior modes, whereas it is the opposite for large values of $|\Gamma|$ (if we exclude box 44). However, there is an important asymmetry between positive and negative values of Γ . Regions dominated by interior modes correspond to negative Γ . In these regions, the correlation between $-\Gamma$ and the surface and interior mode vorticity ratio is 0.75, which indicates that the large-scale gradients are important in determining the relative importance of each mode, as expected. On the other hand, regions dominated by the surface mode correspond mostly to positive Γ . For these regions, the correlation between the interior/surface mode ratio and Γ is only 0.6 (excluding boxes 21, 28, and 44 from the computation of the correlation coefficient).

Since, for negative Γ , the interior modes should dominate the surface signal, the vorticity due to the interior modes should be positively correlated with the observed vorticity at the ocean surface. On the other hand, for positive Γ , the surface mode will dominate. Because the surface buoyancy behaves as a negative PV source $-(f_0/N^2)b_s \delta(z)$ (see Bretherton 1966; Lapeyre and Klein 2006) and in these regions PV' and b'_s are positively correlated (due to $\Gamma > 0$), ψ_{int} and ψ_{sur} will be anticorrelated. Therefore, the vorticity due to the interior modes can be expected to be negatively correlated with the observed vorticity. Figure 13b confirms this reasoning, as it shows that Γ and the correlation of the interior mode vorticity and the observed vorticity taken at $z = 0$ vary in opposite directions. At 460 m, the interior modes begin to dominate the surface-trapped mode and the correlation is positive throughout the Atlantic (not

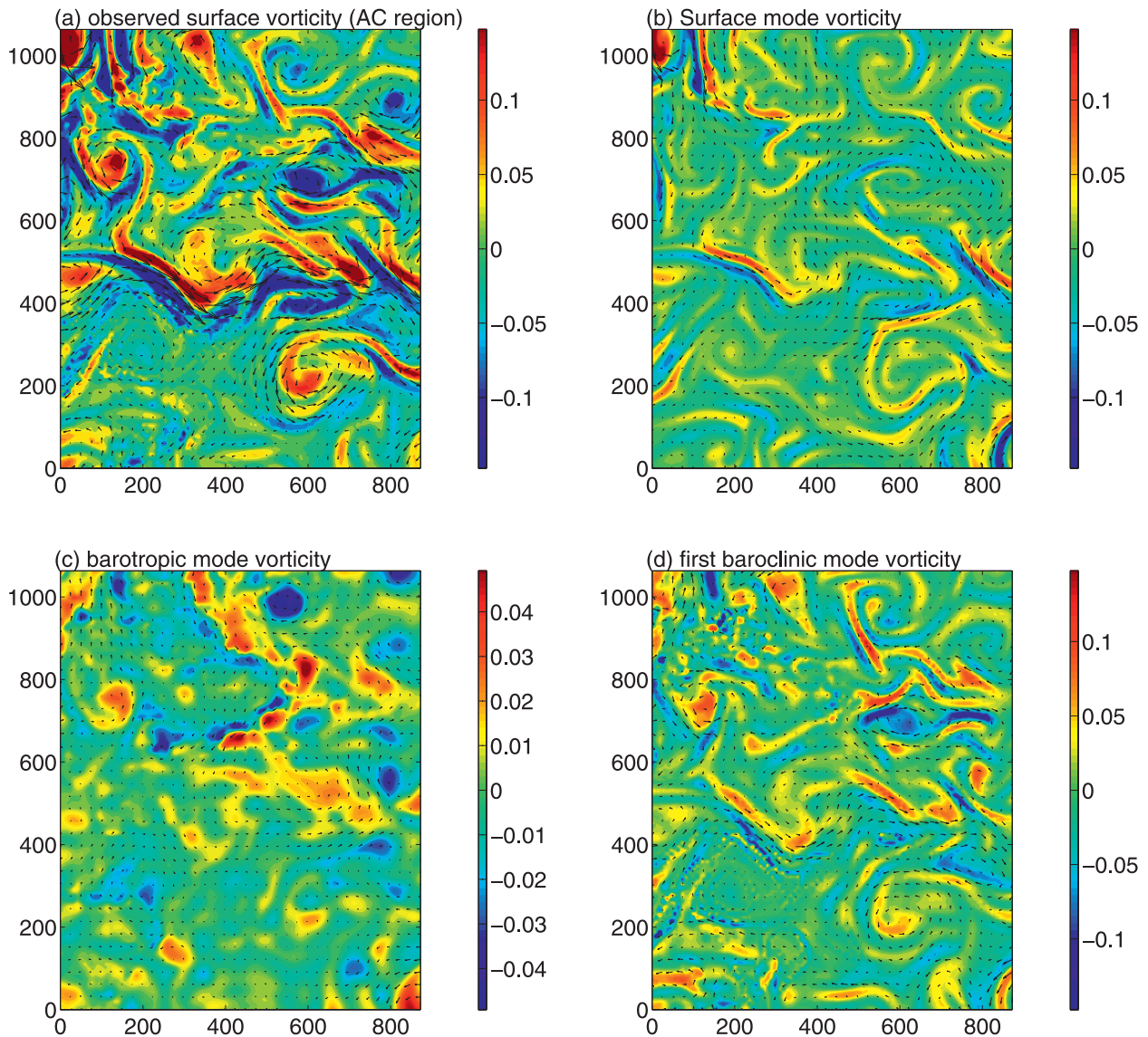


FIG. 8. As in Fig. 4, but for the AC region.

shown). The surface mode has therefore a weak influence at depth.

One could argue that a simpler explanation can be found using linear instability theory. Given Eq. (8), the relative weights of the surface mode and the interior modes might be dependent on the presence or absence of a surface shear. Figure 14 shows the spatial average of the shear $\sqrt{(\partial_z u)^2 + (\partial_z v)^2}/2$ as a function of depth for the three regions studied in detail (Gulf Stream, North Atlantic Drift, Azores Current). If the linear argument was valid, then we would expect the surface shear to be smaller than the interior shear for the Azores Current. This is not observed. The main differences between the three regions are that the shear is stronger in the GS, whereas the two

other regions have shear amplitudes quite smaller, and that the shear in the Azores region decreases more rapidly as a function of depth (not shown). We conclude from this result that shear alone is not able to explain the differences observed in the decomposition and that arguments based on PV inversion seem to be more relevant to explain which mode dominates at the ocean surface.

5. Conclusions

In this paper, it has been shown that the decomposition of a quasigeostrophic flow into barotropic and baroclinic modes is not complete because it contradicts the existence of mesoscale buoyancy anomalies at the

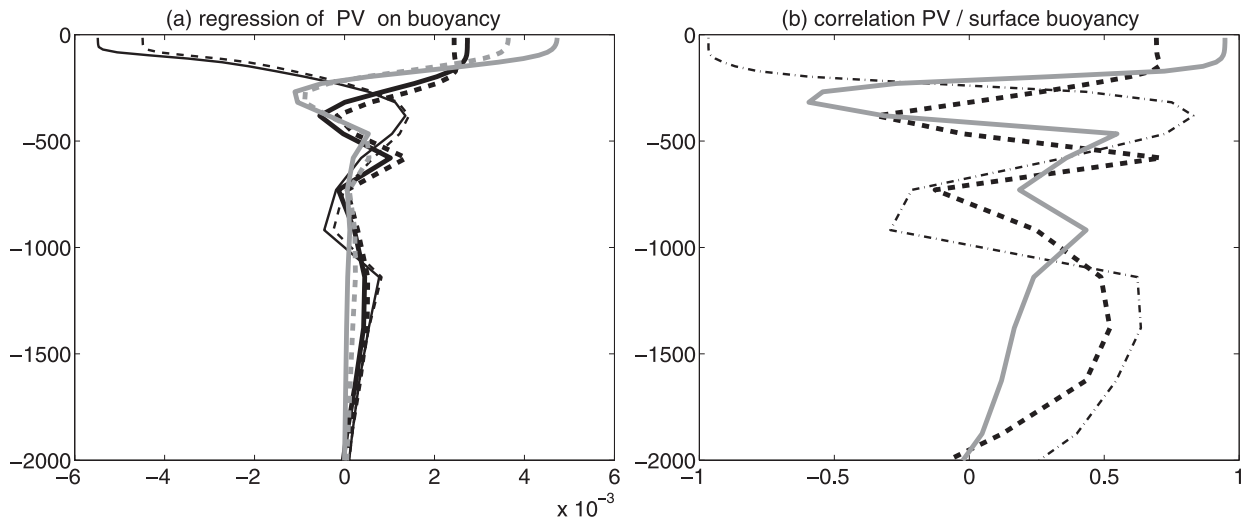


FIG. 12. (a) Regression of $PV'(x, y, z)$ on $b'_s(x, y)$ (solid line) and regression of $\partial_y \overline{PV}(x, y, z)$ on $\partial_y \overline{b}_s(x, y)$ (dashed line) as a function of depth z . (b) Spatial correlation coefficient of $PV'(x, y, z)$ with $b'_s(x, y)$ as a function of depth z . Thick gray curves correspond to the GS region, thin black curves the AC region, and thick black curve the NAD region.

filtered or even noisy in the mesoscale band because it uses along-track data interpolated in space (100 km) and time (1 week). Despite this fact, studies such as Chelton et al. (2007) were able to extract trajectories and a number of eddies throughout the global ocean. The signal at mesoscale seems reliable, at least to have a first indication of the eddy dynamics (also see Stammer 1997). SQG submesoscale structures of 10-km length scale have a time scale of one day. They will certainly be filtered by present altimeter products. Only the eventuality of the Surface Water and Ocean Topography (SWOT) mission could provide, in some years, spatial

high resolution (1 km) of the SSH field. In contrast, SQG mesoscale structures of 100-km length scale have a time scale of 10 days, closer to the time scale of baroclinic and barotropic modes. These structures should be less filtered by the time and space interpolation applied to obtain the altimeter product. This is confirmed by the study of Isern-Fontanet et al. (2006), who showed that microwave SST and altimeter SSH are in SQG balance in the Gulf Stream region for scales between 80 and 300 km. If the OGCM simulation is reliable for mesoscale dynamics, the present study suggests that the velocity field observed at the ocean surface by satellite altimetry

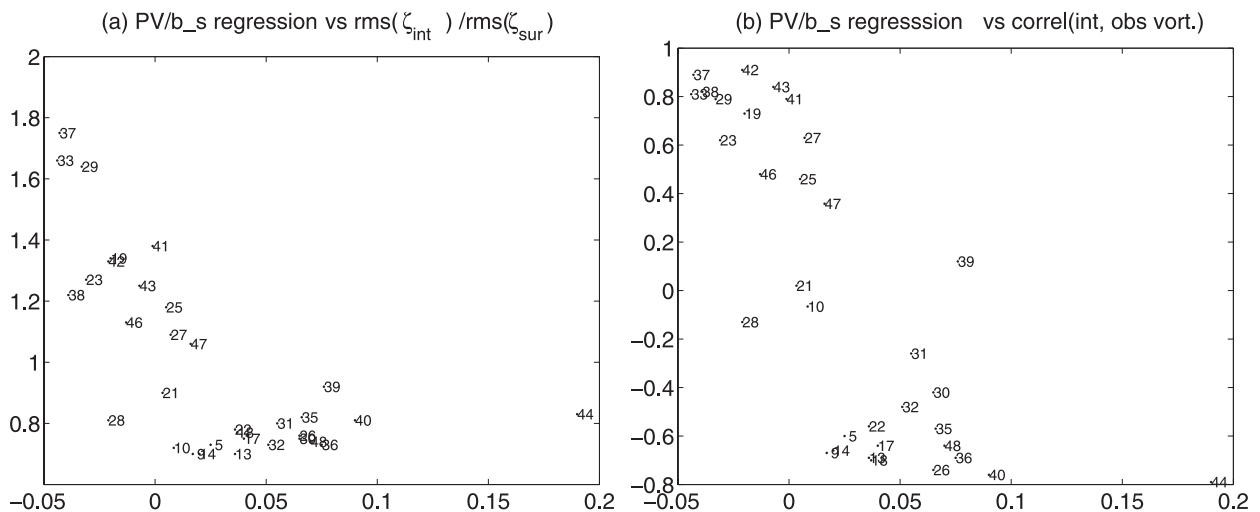


FIG. 13. Scatterplots of Γ (abscissa, km^{-1}) and (a) ratio of rms of ζ_{int} to the rms of ζ_{sur} and (b) correlation coefficient of observed vorticity at surface and interior mode vorticity (ordinate). Each point corresponds to one region of Fig. 10 identified by its number.

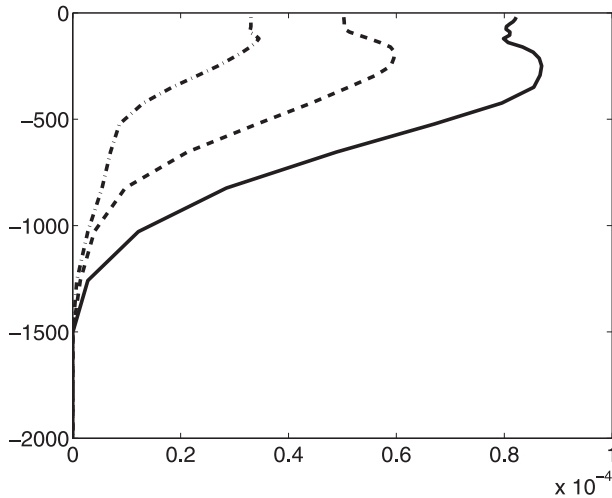


FIG. 14. Spatial mean of the vertical shear as a function of depth for the GS region (continuous), the NAD region (dashed), and the AC region (dashed-dotted).

does not in general reflect the first baroclinic mode, contrary to what has been claimed by different authors (Stammer 1997; Smith and Vallis 2001). It reflects a surface-intensified mode associated with uniform PV and surface buoyancy anomaly, known as a surface QG mode. This strengthens, in part, the applicability of the effective SQG method (Lapeyre and Klein 2006; LaCasce and Mahadevan 2006; Isern-Fontanet et al. 2006, 2008), which is a method based on the surface mode to reconstruct the dynamics of the upper ocean from surface buoyancy using only a constant N^2 .

In conclusion, these results exacerbate the need to understand the coupling between interior PV anomalies and surface buoyancy anomalies, and in particular the observed anticorrelation between the first baroclinic mode and the surface mode. This correlation/anticorrelation is also observed in a simple model coupling SQG dynamics and baroclinic modes in a work by Tulloch and Smith (2009a) to understand the tropopause dynamics. A full theory taking into account both the turbulent cascades associated with interior PV anomalies (Smith and Vallis 2001; Arbic and Flierl 2004; Scott and Arbic 2007) and with surface density anomalies (Held et al. 1995; Capet et al. 2008b) would give a more realistic interpretation of the ocean mesoscale dynamics, as seen in Scott and Wang (2005), Klein et al. (2008), and Capet et al. (2008a).

Acknowledgments. The author wants to acknowledge stimulating discussion about the surface dynamics with Patrice Klein, Shafer Smith, and Rob Scott. In addition, Matthew Hecht and Patrice Klein have provided the numerical simulation used in this paper.

APPENDIX

Technical Aspect of the Decomposition

The streamfunction and buoyancy fields need to be properly balanced to solve (12) and (13) at the same time. In general, this is not strictly true (especially in the mixed layer). To impose thermal wind balance, the method proposed by Rudnick (1996) was followed, which consists in writing

$$\psi(x, y, z) = \phi(x, y) + R(x, y, z) \quad (\text{A1})$$

with

$$R = \frac{1}{f_0} \int_{-H}^z b \, dz. \quad (\text{A2})$$

Here, H is chosen to be $H = 3600$ m. If the functional

$$\int_{-H}^z \iint [(-\partial_y \psi - u_{\text{obs}})^2 + (\partial_x \psi - v_{\text{obs}})^2] \, dx \, dy \, dz \quad (\text{A3})$$

is minimized, a constraint for ϕ is obtained,

$$\nabla^2 \phi = \frac{1}{H} \int_{-H}^0 (\zeta_{\text{obs}} - \nabla^2 R) \, dz. \quad (\text{A4})$$

The streamfunction $\phi + R$ is in thermal wind balance with the buoyancy b : this gives a better result for the reconstruction. It has been checked that the streamfunction $\phi + R$ is very similar to the real one (not shown).

The vertical distribution of $E(K, z)$ using the constraint (17) can be solved numerically using the fact that

$$\frac{\partial E}{\partial z}(z=0) = 1$$

is mathematically equivalent to a Dirac delta function on the rhs of (17) (see Bretherton 1966; Lapeyre and Klein 2006). At the bottom of the ocean, the condition

$$\frac{\partial E}{\partial z}(z=-H) = 0$$

was used, corresponding to no density anomaly there; then decomposition (19) can be discretized and solved through matrix diagonalization. If $E(K, z)$ is projected onto each interior mode F_j , one obtains $n + 1$ equations with $n + 2$ unknowns $[\hat{\alpha}_j(\mathbf{k})$ and $\hat{\gamma}(\mathbf{k})]$,

$$\hat{\alpha}_j(\mathbf{k}) + \hat{\gamma}(\mathbf{k}) \int_{-H}^0 F_j(z) E(K, z) \, dz = \int_{-H}^0 F_j(z) \hat{\psi}(\mathbf{k}, z) \, dz, \quad (\text{A5})$$

for $j = 0$ to n . The last equation is found by minimizing the functional

$$I = \int \int_{z_0}^0 \left| \hat{b}(\mathbf{k}, z) - f_0 \sum_{j=0}^n \hat{\alpha}_j(\mathbf{k}) \frac{\partial F_j}{\partial z}(z) - \hat{\gamma}(\mathbf{k}) f_0 \frac{\partial E}{\partial z}(K, z) \right|^2 dz dK. \quad (\text{A6})$$

Using (A5), one obtains

$$I = \int \int_{z_0}^0 \left| \hat{b}(\mathbf{k}, z) - f_0 \sum_{j=0}^n \hat{\psi}_j(\mathbf{k}) \frac{\partial F_j}{\partial z}(z) - \hat{\gamma}(\mathbf{k}) f_0 \left[\frac{\partial E}{\partial z}(K, z) - \sum_{j=0}^n E_j(K) \frac{\partial F_j}{\partial z}(z) \right] \right|^2 dz dK, \quad (\text{A7})$$

where

$$\hat{\psi}_j(\mathbf{k}) = \int_{-H}^0 F_j(z) \hat{\psi}(\mathbf{k}, z) dz \quad (\text{A8a})$$

and

$$E_j(K) = \int_{-H}^0 F_j(z) E(K, z) dz. \quad (\text{A8b})$$

The minimum of the functional is reached when $DI/D\hat{\gamma}(\mathbf{k}) = 0$; that is,

$$\hat{\gamma}(\mathbf{k}) \int_{z_0}^0 \left| \frac{\partial E}{\partial z}(K, z) - \sum_{j=0}^n E_j(K) \frac{\partial F_j}{\partial z}(z) \right|^2 dz = \int_{z_0}^0 \left[\frac{\hat{b}(\mathbf{k}, z)}{f_0} - \sum_{j=0}^n \hat{\psi}_j(\mathbf{k}) \frac{\partial F_j}{\partial z}(z) \right] \left[\frac{\partial E}{\partial z}(z) - \sum_{j=0}^n E_j(K) \frac{\partial F_j}{\partial z}(z) \right] dz, \quad (\text{A9})$$

which determines $\hat{\gamma}(\mathbf{k})$. As the surface mode is trapped in the upper oceanic layers, the integrals are evaluated between the surface and $z_0 = -400$ m. This method is more robust than a method that would instead use an equation for the buoyancy at a particular level. In this case, the solution is strongly sensitive to the choice of the vertical level (not shown).

The computation of only eight vertical modes ($n = 7$) has been considered because the higher modes are not numerically well resolved (owing to the vertical discretization on 32 levels between the surface and $H = 3600$ m in the POP simulation). The vertical modes have been computed between the surface and $H = 3600$ m. The vertical profiles of the mean N^2 have been smoothed following Emery et al. (1984): N^2 is interpolated on a grid 2.4 times thinner, smoothed with a Gaussian weight over five grid points and then reinterpolated on the original grid. Values of N^2 smaller than 10^{-7} s^{-2} are replaced by 10^{-7} s^{-2} . Finally, E is computed on a grid four times thinner so that the Dirac delta function of PV can be replaced by a step function: then it is interpolated back onto the original grid.

REFERENCES

- Arbic, B. K., and G. R. Flierl, 2004: Baroclinically unstable geostrophic turbulence in the limits of strong and weak bottom Ekman friction: Application to midocean eddies. *J. Phys. Oceanogr.*, **34**, 2257–2273.
- Beckmann, A., 1988: Vertical structure of midlatitude mesoscale instabilities. *J. Phys. Oceanogr.*, **18**, 1354–1371.
- Bishop, C. H., and A. J. Thorpe, 1994: Potential vorticity and the electrostatics analogy: Quasi-geostrophic theory. *Quart. J. Roy. Meteor. Soc.*, **120**, 713–731.
- Brachet, S., P. Y. Le Traon, and C. Le Provost, 2004: Mesoscale variability from a high-resolution model and from altimeter data in the North Atlantic Ocean. *J. Geophys. Res.*, **109**, C12025, doi:10.1029/2004JC002360.
- Bretherton, F. P., 1966: Critical layer instability in baroclinic flows. *Quart. J. Roy. Meteor. Soc.*, **92**, 325–334.
- Bryan, F. O., M. W. Hecht, and R. D. Smith, 2007: Resolution convergence and sensitivity studies with North Atlantic circulation models. Part I: The western boundary current system. *Ocean Modell.*, **16**, 141–159.
- Canuto, C., M. Y. Hussaini, A. Quarteroni, and T. A. Zang Jr., 1988: *Spectral Methods in Fluid Dynamics*. Springer-Verlag, 567 pp.
- Capet, X., P. Klein, B. L. Hua, G. Lapeyre, and J. C. McWilliams, 2008a: Surface kinetic and potential energy transfer in SQG dynamics. *J. Fluid Mech.*, **604**, 165–174.
- , J. C. McWilliams, M. J. Molemaker, and A. F. Shchepetkin, 2008b: Mesoscale to submesoscale transition in the California current system. Part III: Energy balance and flux. *J. Phys. Oceanogr.*, **38**, 2256–2269.
- Charney, J., 1971: Geostrophic turbulence. *J. Atmos. Sci.*, **28**, 1087–1095.
- Chelton, D. B., R. A. De Szoeke, M. G. Schlax, K. El Naggar, and N. Siwertz, 1998: Geographical variability of the first baroclinic Rossby radius of deformation. *J. Phys. Oceanogr.*, **28**, 433–460.
- , M. G. Schlax, R. M. Samelson, and R. A. De Szoeke, 2007: Global observations of large oceanic eddies. *Geophys. Res. Lett.*, **34**, L15606, doi:10.1029/2007GL030812.
- De Mey, P., and A. R. Robinson, 1987: Assimilation of altimeter eddy fields in a limited-area quasi-geostrophic model. *J. Phys. Oceanogr.*, **17**, 2280–2293.

- Dutton, J. A., 1974: The nonlinear quasi-geostrophic equation: Existence and uniqueness of solutions on a bounded domain. *J. Atmos. Sci.*, **31**, 422–433.
- Emery, W. J., W. G. Lee, and L. Magaard, 1984: Geographic and seasonal distributions of Brunt–Väisälä frequency and Rossby radii in the North Pacific and North Atlantic. *J. Phys. Oceanogr.*, **14**, 294–317.
- Flierl, G. R., 1978: Models of vertical structure and the calibration of two-layer models. *Dyn. Atmos. Oceans*, **2**, 341–381.
- Frankignoul, C., and P. Muller, 1979: Quasi-geostrophic response on an infinite β -plane ocean to stochastic forcing by the atmosphere. *J. Phys. Oceanogr.*, **9**, 104–127.
- Gill, A., 1982: *Atmosphere–Ocean Dynamics*. International Geophysical Series, Vol. 30, Academic Press, 662 pp.
- Haines, K., 1991: A direct method for assimilating sea surface height data into ocean models with adjustments to the deep circulation. *J. Phys. Oceanogr.*, **21**, 843–868.
- Held, I. M., R. L. Panetta, and R. T. Pierrehumbert, 1985: Stationary external Rossby waves in vertical shear. *J. Atmos. Sci.*, **42**, 865–883.
- , R. T. Pierrehumbert, S. T. Garner, and K. L. Swanson, 1995: Surface quasi-geostrophic dynamics. *J. Fluid Mech.*, **282**, 1–20.
- Hoskins, B. J., M. E. McIntyre, and A. W. Robertson, 1985: On the use and significance of isentropic potential vorticity maps. *Quart. J. Roy. Meteor. Soc.*, **111**, 877–946.
- Hua, B. L., and D. B. Haidvogel, 1986: Numerical simulations of the vertical structure of quasi-geostrophic turbulence. *J. Atmos. Sci.*, **43**, 2923–2936.
- Isern-Fontanet, J., B. Chapron, G. Lapeyre, and P. Klein, 2006: Potential use of microwave sea surface temperatures for the estimation of ocean currents. *Geophys. Res. Lett.*, **33**, L24608, doi:10.1029/2006GL027801.
- , G. Lapeyre, P. Klein, B. Chapron, and M. W. Hecht, 2008: Three-dimensional reconstruction of oceanic mesoscale currents from surface information. *J. Geophys. Res.*, **113**, C09005, doi:10.1029/2007JC004692.
- Klein, P., and B. L. Hua, 1990: The mesoscale variability of the sea surface temperature: An analytical and numerical model. *J. Mar. Res.*, **48**, 729–763.
- , —, G. Lapeyre, X. Capet, S. Le Gentil, and H. Sasaki, 2008: Upper ocean turbulence from high-resolution 3D simulations. *J. Phys. Oceanogr.*, **38**, 1748–1763.
- LaCasce, J. H., and A. Mahadevan, 2006: Estimating sub-surface horizontal and vertical velocities from sea surface temperature. *J. Mar. Res.*, **64**, 695–721.
- Lapeyre, G., and P. Klein, 2006: Dynamics of the upper oceanic layers in terms of surface quasigeostrophy theory. *J. Phys. Oceanogr.*, **36**, 165–176.
- , —, and B. L. Hua, 2006: Oceanic restratification forced by surface frontogenesis. *J. Phys. Oceanogr.*, **36**, 1577–1590.
- McWilliams, J. C., 1976: Maps from the Mid-Ocean Dynamics Experiment: Part I. Geostrophic streamfunction. *J. Phys. Oceanogr.*, **6**, 810–827.
- , and J. H. S. Chow, 1981: Equilibrium geostrophic turbulence I: A reference solution in a β -plane channel. *J. Phys. Oceanogr.*, **11**, 921–949.
- , W. B. Owens, and B. L. Hua, 1986: An objective analysis of the POLYMODE Local Dynamics Experiment. Part I: General formalism and statistical model selection. *J. Phys. Oceanogr.*, **16**, 483–504.
- Pedlosky, J., 1987: *Geophysical Fluid Dynamics*. 2nd ed. Springer-Verlag, 710 pp.
- Philander, S. G. H., 1978: Forced oceanic waves. *Rev. Geophys.*, **16**, 15–46.
- Rudnick, D. L., 1996: Intensive surveys of the Azores Front. 2. Inferring the geostrophic and vertical velocity fields. *J. Geophys. Res.*, **101**, 16 291–16 303.
- Schlösser, F., and C. Eden, 2007: Diagnosing the energy cascade in a model of the North Atlantic. *Geophys. Res. Lett.*, **34**, L02604, doi:10.1029/2006GL027813.
- Scott, R. B., and F. Wang, 2005: Direct evidence of an oceanic inverse kinetic energy cascade from satellite altimetry. *J. Phys. Oceanogr.*, **35**, 1650–1666.
- , and B. K. Arbic, 2007: Spectral energy fluxes in geostrophic turbulence: Implications for ocean energetics. *J. Phys. Oceanogr.*, **37**, 673–688.
- Siegel, A., J. B. Weiss, J. Toomre, J. C. Mc Williams, P. S. Berloff, and I. Yavneh, 2001: Eddies and vortices in ocean basin dynamics. *Geophys. Res. Lett.*, **28**, 3183–3186.
- Smith, K. S., 2007: The geography of linear baroclinic instability in Earth's oceans. *J. Mar. Res.*, **65**, 655–683.
- , and G. K. Vallis, 2001: The scales and equilibration of mid-ocean eddies: Freely evolving flow. *J. Phys. Oceanogr.*, **31**, 554–571.
- Smith, R., M. Maltrud, F. Bryan, and M. Hecht, 2000: Numerical simulation of the North Atlantic Ocean at $1/10^\circ$. *J. Phys. Oceanogr.*, **30**, 1532–1561.
- Stammer, D., 1997: Global characteristics of ocean variability estimated from regional TOPEX/POSEIDON altimeter measurements. *J. Phys. Oceanogr.*, **27**, 1743–1769.
- Tulloch, R., and K. S. Smith, 2006: A theory for the atmospheric energy spectrum: Depth-limited temperature anomalies at the tropopause. *Proc. Natl. Acad. Sci. USA*, **103**, 14 690–14 694.
- , and —, 2009a: A note on the numerical representation of surface dynamics in quasigeostrophic turbulence: Application to the nonlinear Eady model. *J. Atmos. Sci.*, **66**, 1063–1068.
- , and —, 2009b: Quasigeostrophic turbulence with explicit surface dynamics: Application to the atmospheric energy spectrum. *J. Atmos. Sci.*, **66**, 450–467.
- Tung, K. K., and W. T. Welch, 2001: Remarks on Charney's note on geostrophic turbulence. *J. Atmos. Sci.*, **58**, 2009–2012.
- Wunsch, C., 1997: The vertical partition of oceanic horizontal kinetic energy. *J. Phys. Oceanogr.*, **27**, 1770–1794.